Averaged-Value Modeling and Analysis of 96-Pulse Rectifiers for Harmonic Reduction in Aerospace and HVDC Applications

Sakineh Aghighi [1*]

[1] Department of Electrical Engineering, Institute for Higher Education, ACECR, Hamedan, Iran

*** Corresponding author email address**: s.aghighi@jdhamedan.ac.ir

Received: 2025-06-05 **Revised:** 2025-09-14 **Accepted:** 2025-09-21 **Initial Publish:** 2026-02-15 **Final Publish:** 2026-03-01

Abstract

In recent years, the rapid expansion of More Electric Aircraft systems and high-voltage direct current (HVDC) transmission networks has intensified the demand for power converters that can ensure high power quality with minimal harmonic distortion. Among the well-established solutions, multipulse rectifiers have remained attractive due to their inherent ability to mitigate input current harmonics and improve power factor without the need for complex active filters. Within this family, 96-pulse rectifiers, implemented using double-wound Y/ZYZ transformers or autotransformer-based configurations, offer superior performance by producing nearly sinusoidal waveforms and effectively canceling low-order harmonics. This study develops and analyzes nonlinear averaged-value models for three common 96-pulse rectifier topologies to provide a reliable framework for investigating system dynamics and interactions with constant power loads. A unified generic averaged model is first presented and then tailored to series, parallel, and autotransformer-based structures. The equivalent circuits are derived in such a way that the effects of line resistances, transformer leakage inductances, and interphase reactor (IPR) leakage elements are explicitly included. To validate the accuracy of the proposed models, the averaged-value results are compared with detailed circuit-level simulations conducted in Micro-Cap and, for the autotransformer-based configuration, with prototype experimental tests. The comparisons demonstrate that the proposed models accurately capture both the steady-state operating points and the transient dynamic responses, with deviations of less than a few percent relative to detailed simulations, although high-frequency ripple components are naturally excluded due to the averaging process. Furthermore, the models remain accurate under a wide range of operating conditions, including load variations, changes in source amplitude and frequency, and modifications of DC-link filter parameters. Overall, the results confirm that the developed averaged-value models provide a compact yet accurate analytical tool for the design and performance assessment of high-power multipulse rectifiers in aerospace power systems, uninterruptible power supplies (UPS), and HVDC applications where high efficiency, compactness, and superior power quality are essential.

Keywords: *rectifier-96 pulse-harmonice- Modeling*

How to cite this article:

Aghighi, S. (2026). Averaged-Value Modeling and Analysis of 96-Pulse Rectifiers for Harmonic Reduction in Aerospace and HVDC Applications. Management Strategies and Engineering Sciences, 8(2), 1-20.

1. Introduction

The increasing electrification of transportation systems, particularly in the aerospace sector, has significantly intensified the demand for high-performance power electronic converters that can ensure excellent power quality, high efficiency, and compact design while meeting stringent safety and reliability standards. The concept of the *More Electric Aircraft (MEA)* has emerged as a cornerstone of modern aviation, where conventional hydraulic, pneumatic, and mechanical systems are progressively replaced by electrically powered subsystems to reduce overall weight, improve operational efficiency, and minimize maintenance costs. This shift has, however, introduced substantial challenges to the design of electrical power distribution systems in aircraft, particularly because of the strict requirements on harmonic distortion, electromagnetic compatibility, and the dynamic interaction between power converters and aircraft loads. One of the most persistent issues in such environments is the mitigation

of current harmonics drawn by rectifiers, which constitute the interface between the alternating current (AC) supply and direct current (DC) loads such as motor drives, avionics, and actuation systems. If left uncontrolled, these harmonics can propagate into the aircraft electrical network, leading to overheating of transformers, maloperation of protection systems, reduced efficiency, and, most critically, potential violation of international standards such as IEEE 519 that specify allowable harmonic distortion levels [1-3]. To address these challenges, a wide range of harmonic mitigation techniques have been developed over the past three decades, including active filters, hybrid filters, and improved modulation strategies, but in many aerospace and HVDC applications where reliability and simplicity are paramount, multipulse rectifier systems remain one of the most attractive and widely adopted solutions. Multipulse rectifiers operate by combining the outputs of several phase-shifted diode bridge rectifiers through specially designed transformers or autotransformers such that certain low-order harmonics are naturally canceled, thereby producing nearly sinusoidal input currents with reduced total harmonic distortion (THD) [4, 5]. The performance of a multipulse rectifier is determined by the number of pulses in its output voltage waveform: six-pulse rectifiers are the most basic configuration, while 12-pulse, 18-pulse, 24-pulse, and higher-order systems are developed to achieve progressively better harmonic suppression. While lower-order multipulse systems such as 12-pulse and 18-pulse rectifiers are widely used in medium-power industrial drives, aerospace and HVDC applications increasingly require much stricter harmonic limits that demand higher pulse numbers. This has motivated researchers to explore advanced configurations such as 36-pulse, 48-pulse, 72-pulse, and ultimately 96-pulse rectifiers, which can reduce input current distortion to levels below 5% without the use of additional active filtering stages. Among these, the 96-pulse rectifier is of particular interest due to its ability to achieve very low distortion while maintaining relatively simple diode bridge structures that are robust, reliable, and easy to implement in harsh environments. The key enabling element in 96-pulse systems is the use of phase-shifting devices, either in the form of double-wound transformers (such as Y/ZYZ arrangements) or compact autotransformers, which generate multiple sets of three-phase voltages displaced by precise phase angles (3.75° in this case). By feeding these phase-shifted voltages into multiple six-pulse diode bridges and then combining their outputs in series or parallel, a high-pulse rectified waveform is obtained, which inherently cancels dominant low-order harmonics and leaves only very high-order harmonics that are easier to filter. In aerospace environments, where weight and volume are critical, autotransformer-based configurations are often favored because they achieve the required phase-shifting with reduced size and mass compared to conventional double-wound transformers, although they do so at the cost of losing galvanic isolation [6-9]. Despite the practical advantages of 96-pulse rectifiers, accurately analyzing their dynamic behavior and predicting their performance in complex aircraft or HVDC power systems remains a challenge. Traditional detailed circuit simulations capture switching transients and harmonic content with high fidelity but are computationally intensive, especially when integrated into large system-level models that include multiple converters, transmission lines, and loads. On the other hand, averaged-value models provide a simplified yet powerful analytical framework that represents the essential dynamics of rectifiers over one or more switching intervals while filtering out high-frequency details. Such models are particularly useful for control design, stability analysis, and system-level studies where the focus is on low-frequency dynamics and interactions rather than high-frequency ripple. Previous research has established nonlinear averaged-value models for lower-order multipulse rectifiers, such as 12-pulse, 18-pulse, 24-pulse, and 72-pulse configurations, demonstrating that these models can closely match the behavior of detailed simulations while significantly reducing computational complexity. However, comprehensive averaged-value models for 96-pulse rectifiers have not been extensively developed and validated, particularly in the context of aerospace power systems and HVDC applications. This constitutes a critical research gap because 96-pulse rectifiers are among the most promising solutions for future MEA and HVDC systems, and the lack of compact analytical models hinders efficient system-level design and optimization. The present work addresses this gap by developing and analyzing nonlinear averaged-value models for three representative 96-pulse rectifier topologies: (i) a series-connected double-wound Y/ZYZ transformer-based rectifier, (ii) a parallel-connected double-wound Y/ZYZ transformer-based rectifier employing interphase reactors, and (iii) an autotransformer-based rectifier configuration. The proposed models are derived by averaging the state variables over the fundamental switching interval of 3.75°, thereby producing equivalent DC-side representations that capture the influence of line resistances, transformer leakage inductances, and interphase reactor dynamics. Importantly,

the models provide explicit analytical expressions for the averaged output voltage and equivalent circuit parameters, making them highly suitable for integration into higher-level system studies. To ensure reliability, the models are validated against detailed circuit simulations carried out in Micro-Cap SPICE and, for the autotransformer configuration, further corroborated through experimental prototype tests under various operating conditions. The validation results confirm that the proposed averaged-value models accurately reproduce both the steady-state operating points and transient responses of the rectifiers, with only minor deviations due to the inherent neglect of high-frequency ripple components. Furthermore, the models demonstrate robustness across a range of scenarios, including load step changes, variations in source amplitude and frequency, and different DC-link filter parameter values, thereby establishing their practical applicability for real-world design tasks. The contributions of this study are twofold: first, it extends the body of knowledge on multipulse rectifier modeling by providing the first comprehensive nonlinear averaged-value models for 96-pulse systems, and second, it delivers a validated analytical tool that can significantly accelerate the design and optimization of MEA and HVDC power systems where size, weight, efficiency, and harmonic compliance are of paramount importance [10-13]. By addressing the limitations of previous approaches and filling the identified research gap, this work advances the state of the art in rectifier modeling and paves the way for future studies on multi-rectifier systems, active interphase reactors, and hybrid configurations that combine multipulse rectification with advanced digital control [14-16].

The structure of this paper is organized to guide the reader progressively through the background, methodology, results, and conclusions of the study. The first section presents a comprehensive introduction, emphasizing the importance of power quality in More Electric Aircraft systems and HVDC networks, and highlighting the role of multipulse rectifiers, particularly the 96-pulse configuration. The second section reviews the relevant literature on multipulse rectifiers and averaged-value models, identifying the current research gap and positioning the contribution of this work. The third section describes the research methodology, including the nonlinear averaged-value modeling of the 96-pulse rectifier in three different topologies: series-connected, parallel-connected, and autotransformer-based configurations. This section also provides the mathematical formulations, equivalent circuits, and analytical framework. The fourth section reports the results obtained from detailed circuit simulations and experimental tests, comparing them with the proposed averaged-value models to validate their accuracy. The fifth section provides discussion and analysis of the findings, examining the influence of different topologies, operating conditions, and circuit parameters on rectifier performance. Finally, the sixth section concludes the paper by summarizing the key contributions, outlining the limitations of the study, and suggesting directions for future research.

2. Averaged value model of a generic 96-pulse rectifier

In an effort the unify the treatment of the three 96-pulse systems, the averaging analysis is developed by considering a generic 96-pulse rectifier, shown in Fig. 1. The specific results for each circuit are then obtained by substituting the appropriate terms into the expression for the generic rectifier. In Fig. 1 the AC supply consists of three balanced voltage sources, the line-to-neutral voltages being expressed by the vector $\mathbf{v_s}$, (1).

$$\boldsymbol{v_s} = \begin{bmatrix} v_A \\ v_B \\ v_C \end{bmatrix} = V_m \begin{bmatrix} cos\ \omega\ t \\ cos(\ \omega t - 2\pi/3) \\ cos(\ \omega t + 2\pi/3) \end{bmatrix} \qquad (1)$$

The phase shifting device, which may be a double-wound transformer or an autotransformer, produces two sets of three-phase voltages that are displaced from each other by 3.75°. The two six-pulse rectifiers may be connected in series or parallel to feed the load via the DC-link filter. The three equal inductors L_p represent the primary leakage inductances plus the inductance of the supply lines and the three equal resistors r_p represent the line resistances. The secondary leakage inductances and resistances of the phase-shifting devices are represented by three equal inductors, L_s, and resistors, r_s, respectively in series with each of the inputs to the two rectifiers.Assuming that the input voltages to the two rectifiers are symmetrical, and that each rectifier sees an identical source impedance, then the DC-side waveforms will repeat every 3.75° of the AC supply, giving the characteristic 96-pulse output. Each 3.75° interval begins with an overlap transient in one of the two bridges as the DC-link current commutates between diodes, whilst in the second part of the 3.75° interval only two diodes in each bridge are in conduction. To derive the averaged model the state variables are therefore averaged across a 3.75° interval of the AC supply. For simplicity the overlap angle is assumed to be small and each rectifier output voltage may therefore be described by a single equation within the 3.75° switching interval, only two diodes being in conduction in

each bridge. This is justified since the more detailed analysis of the six pulse rectifier in Chapter 2 showed that for some realistic values of parameters in a rectifier the effect of the overlap on the model values is small and negligible. First we will derive a general expression for the overall rectifier output voltage.

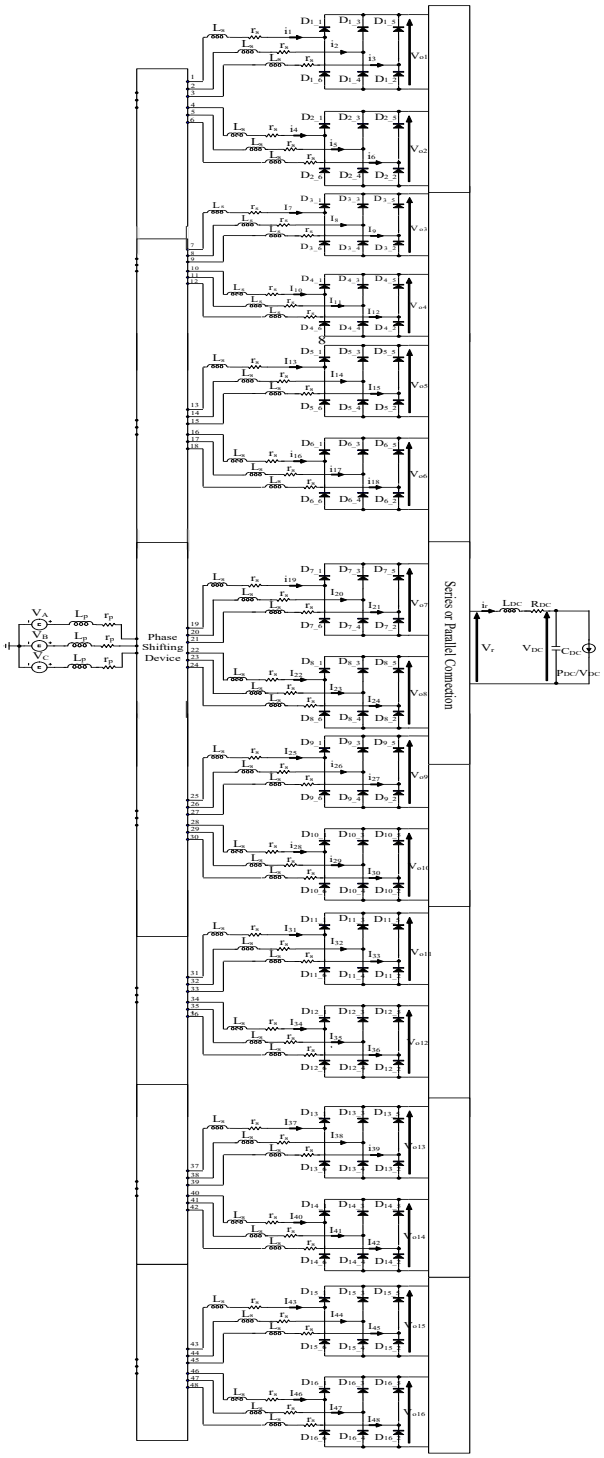

Figure 1. A generic 96-pulse rectifier with DC link filter and constant power load

Within a specific 3.75° interval the individual rectifier output voltages V_{o1} and V_{o2} and V_{o16} may be expressed by a matrix equation of the form:

$$V_{o1}, V_{o2}, V_{o16} = f(\boldsymbol{v_s}, \boldsymbol{i_U}, \boldsymbol{i_L}, \ldots, \boldsymbol{i_z}) \quad (2)$$

$\mathbf{v_s}$ is the source voltage vector, (1), and $\mathbf{i_U}$ and $\mathbf{i_L}$ are vectors of the 16 bridge input currents:

$$\boldsymbol{i_U} = I_1 = [i_1 \quad i_2 \quad i_3]^T \quad (3)$$

$$\boldsymbol{i}_2 = [i_4 \quad i_5 \quad i_6]^T \quad (4)$$

$$\boldsymbol{i}_{16} = [i_{46} \quad i_{47} \quad i_{48}]^T \quad (5)$$

The overall rectifier output voltage, V_r, is obtained by appropriate combination of V_{o1} and V_{o2},… summation for a series connection, and for parallel connection, one or two inter-phase reactors must be used and V_r is the mean value of V_{o1} and $V_{o16}$with the inter-phase reactor leakage inductance appearing as a series inductance. Therefore, within a specific 3.75° interval the overall rectifier output voltage V_r may be expressed generally as:

(6)

$$\begin{bmatrix} Vo_1 \\ Vo_2 \\ Vo_3 \\ Vo_4 \\ Vo_5 \\ Vo_6 \\ Vo_7 \\ Vo_8 \\ Vo_9 \\ Vo_{10} \\ Vo_{11} \\ Vo_{12} \\ Vo_{13} \\ Vo_{14} \\ Vo_{15} \\ Vo_{16} \end{bmatrix} = A_1 v_s - B_1 \frac{d}{dt}(i_1) - B_2 \frac{d}{dt}(i_2) - B_3 \frac{d}{dt}(i_3) - B_4 \frac{d}{dt}(i_4) - B_5 \frac{d}{dt}(i_5) - B_6 \frac{d}{dt}(i_6) - B_7 \frac{d}{dt}(i_7) - B_8 \frac{d}{dt}(i_8) - B_9 \frac{d}{dt}(i_9)$$

$$- B_{10} \frac{d}{dt}(i_{10}) - B_{11} \frac{d}{dt}(i_{11}) - B_{12} \frac{d}{dt}(i_{12}) - B_{13} \frac{d}{dt}(i_{13}) - B_{14} \frac{d}{dt}(i_{14}) - B_{15} \frac{d}{dt}(i_{15}) - B_{16} \frac{d}{dt}(i_{16}) - C \frac{d}{dt}(i_L)$$

where:

$$\boldsymbol{L} = [L_p \quad L_s] \boldsymbol{r} = [r_p \quad r_s] \quad (7)$$

i_r is the DC link current, and **A**, $\mathbf{B_1}$,… $\mathbf{B_{16}}$ and **C** are coefficient matrices, and depend on the phase shifting device and the analysis interval. The value of D depends on the connection of the bridge outputs and the arrangement of the Inter-Phase Reactors (IPR). D is zero if there are no IPRs.The detailed analysis of the three 96-pulse converters is presented in Appendices 3,4 and 6, showing that the overall output voltage may be expressed by an equation of the form of equation (5).The local averaged output voltage $\bar{V}_r$within 3.75° switching period is determined by integrating (5) over the 3.75° period, expressed generally here as the interval$\theta_1 \leq \theta \leq \theta_2$, and then dividing by the time, giving (8)

$$\bar{V}_r = \frac{1}{(\theta_2 - \theta_1)/\omega} \int_{\theta_1/\omega}^{\theta_2/\omega} \mathbf{A} \mathbf{v}_s dt - \mathbf{L}\mathbf{B}_{1,2,\ldots 16} \left[\frac{\mathbf{i}_U(\theta_2/\omega) - \mathbf{i}_U(\theta_1/\omega)}{(\theta_2 - \theta_1)/\omega} \right] - \mathbf{L}\mathbf{C}_{1,2,\ldots 16} \left[\frac{\mathbf{i}_L(\theta_2/\omega) - \mathbf{i}_L(\theta_1/\omega)}{(\theta_2 - \theta_1)/\omega} \right]$$

$$- \mathbf{r}\mathbf{B}_{1,2,\ldots 16} \frac{1}{\Delta t} \int_{\theta_1/\omega}^{\theta_2/\omega} \mathbf{i}_U(\theta/\omega) dt - \mathbf{r}\mathbf{C}_{1,2,\ldots 16} \frac{1}{\Delta t} \int_{\theta_1/\omega}^{\theta_2/\omega} \mathbf{i}_L(\theta/\omega) dt - D \frac{d\bar{i}_r}{dt} \quad (8)$$

where $d\bar{\imath}_r/dt$ is the rate of change of the DC-link current, assumed constant, within the switching period.

The average voltage drops across the inductive components, the second and the third terms in equation (8) are seen to be directly related to the current changes in those components, and to determine the average voltage drop across the resistive components, the change in load current within the 3.75° switching period is assumed to be negligibly small, therefore equation (8) becomes:

$$\bar{V}_r = \frac{1}{(\theta_2-\theta_1)/\omega}\int_{\theta_1/\omega}^{\theta_2/\omega}\mathbf{A}\mathbf{v}_s dt - \mathbf{L}\mathbf{B}_{1,2,\ldots16}\left[\frac{\mathbf{i}_U(\theta_2/\omega)-\mathbf{i}_U(\theta_1/\omega)}{(\theta_2-\theta_1)/\omega}\right]$$
$$-\mathbf{L}\mathbf{C}_{1,2,\ldots16}\left[\frac{\mathbf{i}_L(\theta_2/\omega)-\mathbf{i}_L(\theta_1/\omega)}{(\theta_2-\theta_1)/\omega}\right]-\mathbf{r}\mathbf{B}_{1,2,\ldots16}\mathbf{i}_U(\theta_2/\omega)-\mathbf{r}\mathbf{C}_{1,2,\ldots16}\mathbf{i}_L(\theta_2/\omega)-D\frac{d\bar{\imath}_r}{dt} \quad (9)$$

In this analysis it is assumed that the three phase input to the upper bridge leads the input to the lower one by 3.75°, the 3.75° averaging interval begins at $\theta_1$when the load current starts to commutate from D2_1 to D2_3 in the lower bridge, and the interval ends at $\theta_2$when the current commutation from D1_2 to D1_6 begins in the upper bridge.

The DC-link current at the start of the interval is assumed to be $\bar{\imath}_r$, which is the local average value and during the interval the DC link current rises linearly by an amount Δi. Based on these assumptions the current vectors $\mathbf{i}_U$ and $\mathbf{i}_L$ will therefore have the initial and final values in (10) and (11).

$$\boldsymbol{i_U}(\theta_1/\omega) = k_o\begin{bmatrix}0\\ \bar{\imath}_r\\ -\bar{\imath}_r\end{bmatrix} \qquad \boldsymbol{i_U}(\theta_2/\omega) = k_o\begin{bmatrix}0\\ \bar{\imath}_r+\Delta i\\ -\bar{\imath}_r-\Delta i\end{bmatrix} \quad (10)$$

$$\boldsymbol{i_L}(\theta_1/\omega) = k_o\begin{bmatrix}\bar{\imath}_r\\ 0\\ -\bar{\imath}_r\end{bmatrix} \qquad \boldsymbol{i_L}(\theta_2/\omega) = k_o\begin{bmatrix}0\\ \bar{\imath}_r+\Delta i\\ -\bar{\imath}_r-\Delta i\end{bmatrix} \quad (11)$$

The constant k_o is unity when the two bridge outputs are connected in series, and has a value of 0.5 when the outputs are in parallel.

By substituting the initial and final values of the current vectors, (10) and (11), into (9), the expression for the averaged output voltage of the rectifier is:

$$\bar{V}_r = \frac{96\omega}{\pi}\mathbf{A}\int_{\theta_1/\omega}^{\theta_2/\omega}\mathbf{v}_s dt - \frac{96\omega}{\pi}k_o\mathbf{L}\mathbf{B}_{1,2,\ldots16}\begin{bmatrix}0\\ \Delta i\\ -\Delta i\end{bmatrix} - \frac{96\omega}{\pi}k_o\mathbf{L}\mathbf{C}_{1,2,\ldots16}\begin{bmatrix}-\bar{\imath}_r\\ \bar{\imath}_r+\Delta i\\ \Delta i\end{bmatrix}$$
$$-k_o\mathbf{r}\mathbf{B}_{1,2,\ldots16}\begin{bmatrix}0\\ \bar{\imath}_r\\ -\bar{\imath}_r\end{bmatrix} - k_o\mathbf{r}\mathbf{C}_{1,2,\ldots16}\begin{bmatrix}0\\ \bar{\imath}_r\\ -\bar{\imath}_r\end{bmatrix} - D\frac{d\bar{\imath}_r}{dt} \quad (12)$$

By substituting $\Delta i = \frac{\pi}{96\omega}\frac{d\bar{\imath}_r}{dt}$and collecting terms, the final expression for $\bar{V}_r$ is:

$$\bar{V}_r = \frac{96\omega}{\pi}\mathbf{A}\int_{\theta_1/\omega}^{\theta_2/\omega}\mathbf{v}_s dt - \frac{96\omega}{\pi}k_o\mathbf{L}\mathbf{C}_{1,2,\ldots16}\begin{bmatrix}-1\\ 1\\ 0\end{bmatrix}\bar{\imath}_r - \left(k_o\mathbf{L}\left(\mathbf{B}_{1,2,\ldots16}+\mathbf{C}_{1,2,\ldots16}\right)\begin{bmatrix}0\\ 1\\ -1\end{bmatrix}+D\right)\frac{d\bar{\imath}_r}{dt}$$
$$-\left(k_o\mathbf{r}\left(\mathbf{B}_{1,2,\ldots16}+\mathbf{C}_{1,2,\ldots16}\right)\begin{bmatrix}0\\ 1\\ -1\end{bmatrix}\right)\bar{\imath}_r \quad (13)$$

$$\left(\boldsymbol{B}=\boldsymbol{B}_{1,2,\ldots16},\boldsymbol{C}=\boldsymbol{C}_{1,2,\ldots16}\right) \quad (14)$$

for the switching interval in which diodes D2_3, D2_2 and D1_3, D1_2 are in conduction. The first part of right side of equation (13) shows the ideal output voltage. The second part shows the overlap resistor term. The third term is due to the AC line inductors and IPR leakage inductance. The last part shows a resistive voltage drop which is related to the AC line resistor values. This general equation for the averaged DC output of a 96-pulse rectifier for the specific conduction interval considered is applied in the following section to three different circuit configurations.

3. Averaged value model of alternative 96-pulse rectifiers

The expressions for **A**, **B**, **C**, D, k_o, θ_1 and θ_2 are different for each of the three common 96-pulse rectifiers and the circuits are discussed in turn in the next sections, in each case, the analysis is conducted for the 3.75° interval that starts with the commutation from D2_1 to D2_3 and ends with the commutation from D1_2 to D1_6, as analysed in generic circuit considered in paper 72.

4. Series Y/ZYZΔ connection

Figure 2 shows the diagram of a series connected doubly-wound, transformer-based, 96-pulse rectifier with a constant power load. The ratio *1: n* is the effective turn ration of the overall three-phase transformer, it relates the input and the output line-to-line voltages and does not include the $1:\frac{\sqrt{3}}{3}$ ratio of the Y/ZYZΔ windings.

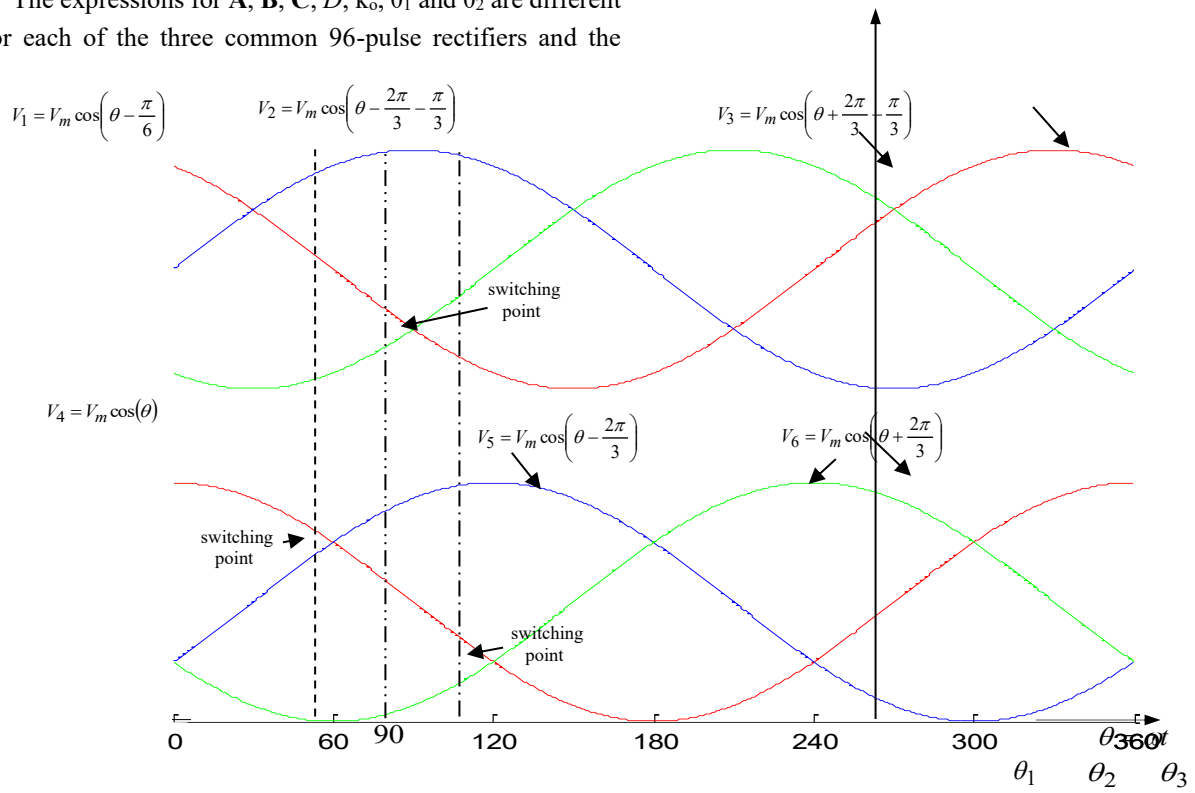

Figure 2. Two 3-phase output voltages of a doubly-wound transformer

Fig. 3 shows the output voltages of the doubly wound transformer. According to the line voltages shown in Fig. 3, the values of θ_1 andθ_2 are 60° and 90° respectively for the 30° interval which starts with the commutation from D2_1 to D2_3 and ends with the commutation from D1_2 to D1_6.In a series connection an IPR is not required, therefore $D = 0$in (3-5) and the constant k_o in (10) and (11) is unity. The values of the terms in equation (5) for this circuit are determined in Previous article and the results are:

series Y/ZYZΔ 96-pulse rectifier				
A	$[\ \frac{1}{\sqrt{3.27}}$	$(\frac{.26}{\sqrt{3.27}})$	$-(1+\frac{3.73}{\sqrt{2}})\ ]$	

B1	$\left[(1+\frac{4L_p}{\sqrt{3.27}}) \right.$	$-(1+\frac{.26}{\sqrt{3}})L_p+3L_s$	$\left. -((1+\frac{3.73}{\sqrt{3.27}})L_p+3L_s) \right]$	
B2	$\left[\frac{3L_p}{\sqrt{3.27}} \right.$	$-(1+\frac{.26}{\sqrt{3.27}})L_p+4L_s$	$\left. -((1+\frac{.26}{\sqrt{3.27}})L_p+2L_s) \right]$	
B3	$(1+\frac{1}{\sqrt{3.27}})$	$-(1+\frac{1}{\sqrt{3.27}})$	$\frac{1}{.26}(1+\frac{1}{\sqrt{3.27}})$	
B4	$-(1+\frac{1}{\sqrt{3.27}}\frac{Lp}{4}+\frac{L_s}{4})$	$-(1+\frac{1}{\sqrt{3.27}}\frac{Lp}{4})$	$(1+\frac{Lp}{\sqrt{3.27}})$	
B5	$\left[(1+\frac{4L_p}{\sqrt{3.27}}) \right.$	$-(1+\frac{.26}{\sqrt{3}})L_p+3L_s$	$\left. -((1+\frac{3.73}{\sqrt{3.27}})L_p+3L_s) \right]$	
B6	$\left[\frac{3L_p}{\sqrt{3.27}} \right.$	$-(1+\frac{.26}{\sqrt{3.27}})L_p+4L_s$	$\left. -((1+\frac{.26}{\sqrt{3.27}})L_p+2L_s) \right]$	
B7	$(1+\frac{1}{\sqrt{3.27}})$	$-(1+\frac{1}{\sqrt{3.27}})$	$\frac{1}{.26}(1+\frac{1}{\sqrt{3.27}})$	
B8	$-(1+\frac{1}{\sqrt{3.27}}\frac{Lp}{4}+\frac{L_s}{4})$	$-(1+\frac{1}{\sqrt{3.27}}\frac{Lp}{4})$	$(1+\frac{Lp}{\sqrt{3.27}})$	
B9	$\left[(1+\frac{4L_p}{\sqrt{3.27}}) \right.$	$-(1+\frac{.26}{\sqrt{3}})L_p+3L_s$	$\left. -((1+\frac{3.73}{\sqrt{3.27}})L_p+3L_s) \right]$	
B10	$\left[\frac{3L_p}{\sqrt{3.27}} \right.$	$-(1+\frac{.26}{\sqrt{3.27}})L_p+4L_s$	$\left. -((1+\frac{.26}{\sqrt{3.27}})L_p+2L_s) \right]$	
B11	$(1+\frac{1}{\sqrt{3.27}})$	$-(1+\frac{1}{\sqrt{3.27}})$	$\frac{1}{.26}(1+\frac{1}{\sqrt{3.27}})$	
B12	$-(1+\frac{1}{\sqrt{3.27}}\frac{Lp}{4}+\frac{L_s}{4})$	$-(1+\frac{1}{\sqrt{3.27}}\frac{Lp}{4})$	$(1+\frac{Lp}{\sqrt{3.27}})$	
B13	$\left[(1+\frac{4L_p}{\sqrt{3.27}}) \right.$	$-(1+\frac{.26}{\sqrt{3}})L_p+3L_s$	$\left. -((1+\frac{3.73}{\sqrt{3.27}})L_p+3L_s) \right]$	
B14	$\left[\frac{3L_p}{\sqrt{3.27}} \right.$	$-(1+\frac{.26}{\sqrt{3.27}})L_p+4L_s$	$\left. -((1+\frac{.26}{\sqrt{3.27}})L_p+2L_s) \right]$	
B15	$(1+\frac{1}{\sqrt{3.27}})$	$-(1+\frac{1}{\sqrt{3.27}})$	$\frac{1}{.26}(1+\frac{1}{\sqrt{3.27}})$	
B16	$-(1+\frac{1}{\sqrt{3.27}}\frac{Lp}{4}+\frac{L_s}{4})$	$-(1+\frac{1}{\sqrt{3.27}}\frac{Lp}{4})$	$(1+\frac{Lp}{\sqrt{3.27}})$	
C	$\frac{2.26L_p}{4\sqrt{3.27}}$	$-(1+\frac{1}{\sqrt{3.27}}\frac{L_p}{4}+\frac{3L_s}{4})$	$((1+\frac{1}{\sqrt{3.27}})\frac{L_p}{4})$	
$\boldsymbol{\theta_1}$,$\boldsymbol{\theta_2}$, *IPR*, $\boldsymbol{i}$	$\frac{\pi}{3}+\frac{\pi}{36}$	$\frac{\pi}{2}+\frac{\pi}{36}$	0	i_L

Substituting the appropriate values into (13) and simplifying yields:

$$\overline{V_r}=\frac{96\sqrt{3}nV_m}{\pi}-\left[\frac{96\omega n^2(L_p+L_s)}{\pi}\right]\bar{\imath}_r-\left[4\left(1+\frac{\sqrt{3}}{2}\right)n^2L_p+4L_s\right]\frac{d\bar{\imath}_r}{dt}-\left[4\left(1+\frac{\sqrt{3}}{2}\right)n^2r_p+4r_s\right]\bar{\imath}_r \quad (15)$$

As expected, the averaged output voltage comprises a constant voltage term, a "resistive" volt drop, which is due to overlap effects, an inductive element and a resistive volt drop due to the line resistors. Using (15), an averaged, DC-side equivalent circuit may be drawn for the rectifier. Fig. 4 shows the average model. The expressions for the component values in the equivalent circuit are given in Table 1.

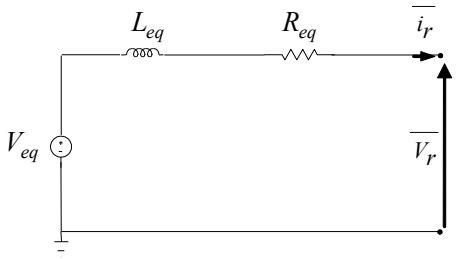

Figure 3. Averaged model of a 96-pulse rectifier

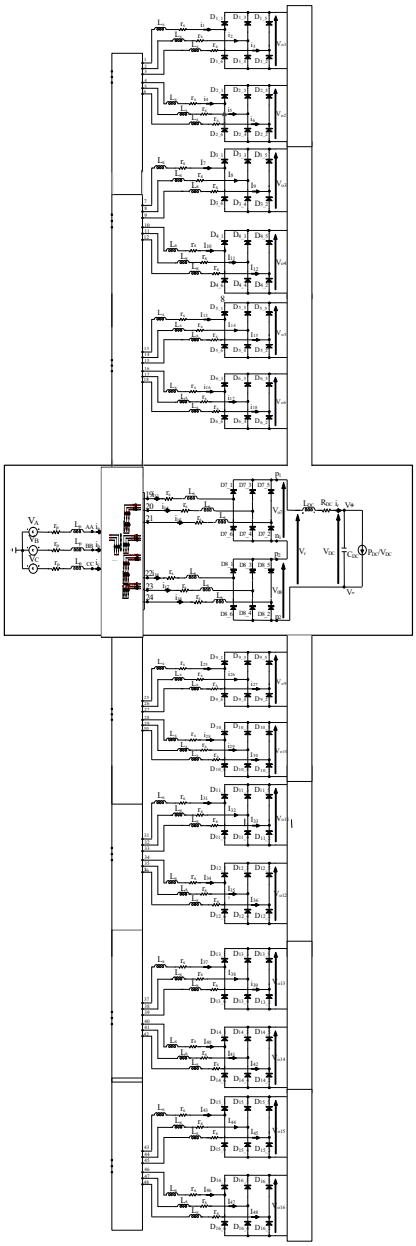

Figure 4. Series connected doubly-wound transformer-based Y/ZYZ□, 96-pulse rectifier with constant power load

Table 1. Terms of the averaged model of a series Y/ZYZ□ 96-pulse rectifier

V_{eq}	R_{eq}	L_{eq}
$\frac{96\sqrt{3}n}{\pi}V_m$	$\frac{96\omega}{\pi}(n^2L_p+L_s)+4\left[\left(1+\frac{\sqrt{3}}{2}\right)n^2r_p+r_s\right]$	$4\left[\left(1+\frac{\sqrt{3}}{2}\right)n^2L_p+L_s\right]$

5. Parallel Y/ZYZΔ connection

When the two rectifiers are connected in a parallel, doubly-wound, transformer-based, 96-pulse rectifier an IPR is required to support the instantaneous voltage difference in the two outputs. Figure 5 shows the diagram of the parallel, doubly-wound, transformer-based, 96-pulse rectifier. The overall transformer turns ratio is again assumed to be $1:n$.

Because of the IPR, the diode bridges will, ideally, share the load current, therefore, the constant k_o in (10) and (11) has the value 0.5 and D in (5) is equal to L_{ipr}, the leakage inductance of the IPR. Since the transformer connection in this circuit is identical to that used for the series configured rectifier section, the bridge input voltages are the same as those in Fig. 3. The expressions for the terms in equation (5) for this circuit are calculated in Previous article and they are:

	Parallel connected 96-pulse rectifier with constant power load
A	$(1+\frac{1}{.26\sqrt{3.27}})\quad -\frac{1}{.26}(1+\frac{1}{\sqrt{3.27}})\quad \frac{1}{.26}(1+\frac{3.73}{\sqrt{3.27}})$
B1	$(1+\frac{.26}{\sqrt{3.27}})\frac{L_p}{4}+\frac{L_s}{4}-((1+\frac{.26}{\sqrt{3.27}})\frac{L_p}{4})\quad (1+\frac{L_p}{\sqrt{3.27}})$
B2	$\frac{-3L_p}{4\sqrt{3.27}}\quad -(1+\frac{.26}{\sqrt{3.27}})\frac{L_p}{4}+\frac{3L_s}{4}\quad -((1+\frac{1}{\sqrt{3.27}})\frac{L_p}{4})$
B3	$\left[\ (1+\frac{L_p}{\sqrt{3.27}})\quad -(1+\frac{1}{\sqrt{3}})L_p\quad ((1+\frac{1}{\sqrt{3.27}})L_p)\ \right]$
B4	$(1+\frac{.26}{\sqrt{3.27}})\frac{L_p}{4}+\frac{L_s}{4}-((1+\frac{.26}{\sqrt{3.27}})\frac{L_p}{4})\quad (1+\frac{L_p}{\sqrt{3.27}})$
B5	$\frac{-3L_p}{4\sqrt{3.27}}\quad -(1+\frac{.26}{\sqrt{3.27}})\frac{L_p}{4}+\frac{3L_s}{4}\quad -((1+\frac{1}{\sqrt{3.27}})\frac{L_p}{4})$
B6	$\left[\ (1+\frac{L_p}{\sqrt{3.27}})\quad -(1+\frac{1}{\sqrt{3}})L_p\quad ((1+\frac{1}{\sqrt{3.27}})L_p)\ \right]$
B7	$(1+\frac{.26}{\sqrt{3.27}})\frac{L_p}{4}+\frac{L_s}{4}-((1+\frac{.26}{\sqrt{3.27}})\frac{L_p}{4})\quad (1+\frac{L_p}{\sqrt{3.27}})$
B8	$\frac{-3L_p}{4\sqrt{3.27}}\quad -(1+\frac{.26}{\sqrt{3.27}})\frac{L_p}{4}+\frac{3L_s}{4}\quad -((1+\frac{1}{\sqrt{3.27}})\frac{L_p}{4})$
B9	$\left[\ (1+\frac{L_p}{\sqrt{3.27}})\quad -(1+\frac{1}{\sqrt{3}})L_p\quad ((1+\frac{1}{\sqrt{3.27}})L_p)\ \right]$
B10	$(1+\frac{.26}{\sqrt{3.27}})\frac{L_p}{4}+\frac{L_s}{4}-((1+\frac{.26}{\sqrt{3.27}})\frac{L_p}{4})\quad (1+\frac{L_p}{\sqrt{3.27}})$
B11	$\frac{-3L_p}{4\sqrt{3.27}}\quad -(1+\frac{.26}{\sqrt{3.27}})\frac{L_p}{4}+\frac{3L_s}{4}\quad -((1+\frac{1}{\sqrt{3.27}})\frac{L_p}{4})$
B12	$\left[\ (1+\frac{L_p}{\sqrt{3.27}})\quad -(1+\frac{1}{\sqrt{3}})L_p\quad ((1+\frac{1}{\sqrt{3.27}})L_p)\ \right]$
B13	$\left[\ (1+\frac{L_p}{\sqrt{3.27}})\quad -(1+\frac{1}{\sqrt{3}})L_p\quad ((1+\frac{1}{\sqrt{3.27}})L_p)\ \right]$
B14	$(1+\frac{.26}{\sqrt{3.27}})\frac{L_p}{4}+\frac{L_s}{4}-((1+\frac{.26}{\sqrt{3.27}})\frac{L_p}{4})\quad (1+\frac{L_p}{\sqrt{3.27}})$
B15	$\frac{-3L_p}{4\sqrt{3.27}}\quad -(1+\frac{.26}{\sqrt{3.27}})\frac{L_p}{4}+\frac{3L_s}{4}\quad -((1+\frac{1}{\sqrt{3.27}})\frac{L_p}{4})$
B16	$\left[\ (1+\frac{L_p}{\sqrt{3.27}})\quad -(1+\frac{1}{\sqrt{3}})L_p\quad ((1+\frac{1}{\sqrt{3.27}})L_p)\ \right]$
C	$[-\frac{L_p}{\sqrt{3.27}}\quad -(1+\frac{1}{\sqrt{3.27}}L_p+4L_s)\quad -(1+\frac{1}{\sqrt{3.27}}L_p+2L_s)\quad]$
θ_1,θ_2, D, i	$\frac{\pi}{3}+\frac{\pi}{48}\quad \frac{\pi}{2}+\frac{\pi}{48}\quad 16L_{IPRr}\quad i_L/16$

Substituting these values into (13) and simplifying results in:

$$\overline{V_r} = \frac{48\sqrt{3}nV_m}{\pi} - \left[\frac{48\omega\left(n^2L_p+L_s\right)}{2\pi}\right]\bar{\imath}_r - \left[\left(1+\frac{\sqrt{3}}{2}\right)n^2L_p + L_s + L_{ipr}\right]\frac{d\bar{\imath}_r}{dt} - \left[\left(1+\frac{\sqrt{3}}{2}\right)n^2r_p + r_s\right]\bar{\imath}_r \quad (19)$$

The expression for $\bar{V}_r$ has the same form as (18) for the series connected rectifier, but with small differences. The equivalent circuit is the same as shown in Fig. 4. The expressions for the component values in the equivalent circuit are given in Table 2.

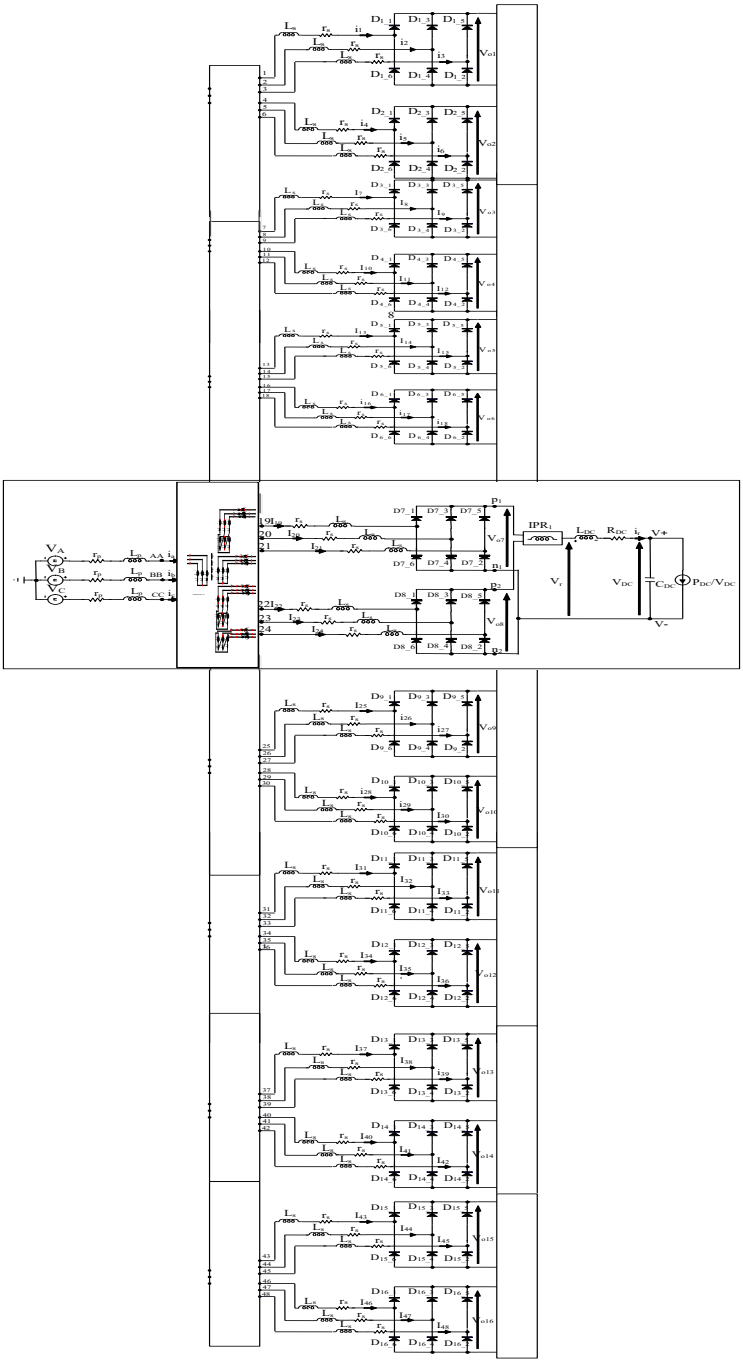

Figure 5. Parallel connected doubly-wound, transformer-based, 96-pulse rectifier with constant power load

Table 2. Terms of the averaged model of a parallel Y/ZYZ□ 96-pulse rectifier

V_{eq}	R_{eq}	L_{eq}
$\frac{48\sqrt{3}n}{\pi}V_m$	$\frac{48\omega}{2\pi}(n^2L_p+L_s)+\left[\left(1+\frac{\sqrt{3}}{2}\right)n^2r_p+r_s\right]$	$\left[\left(1+\frac{\sqrt{3}}{2}\right)n^2L_p+L_s\right]+L_{ipr}$

6. Autotransformer-based rectifier

Fig. 6 shows the autotransformer-based 96-pulse rectifier. The autotransformer produces two sets of three-phase waveforms that are phase shifted by ±3.75° with respect to the AC supply, and it is shown in reference [4, 5] that the autotransformer turns-ratio k:1 must be 26.64:1 ($k = \sqrt{3}/tan\,3.75°$) to produce the appropriately phase shifted outputs. Since the lower diode bridge input voltages are now delayed by 3.75° compared with the previous two circuits, the values of θ_1 and θ_2 are now 75° and 105° respectively.

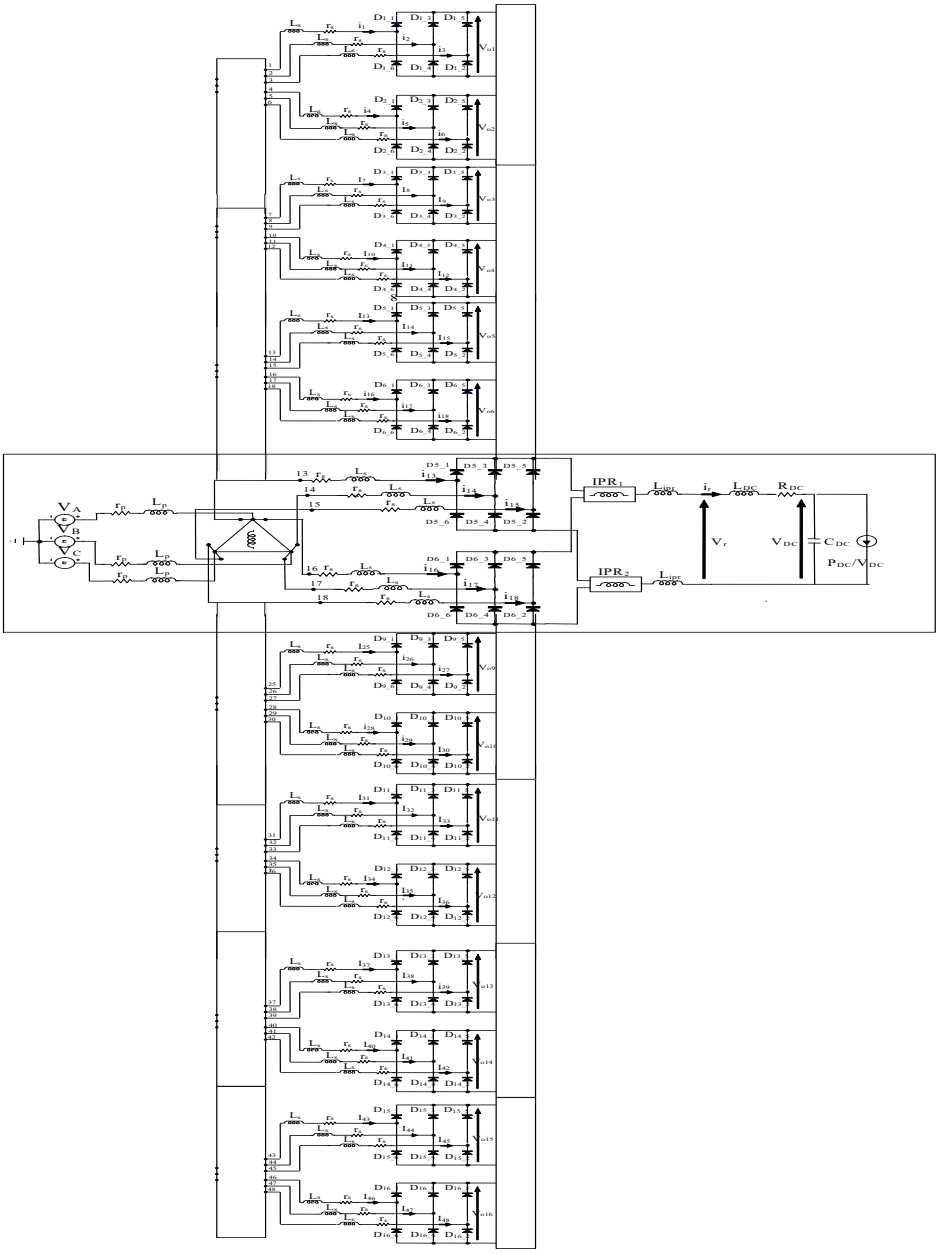

Figure 6. Autotransformer based 96-pulse rectifier with DC link and constant power load

Figure 7 shows the two 3-phase sets of the output voltages of the autotransformer and also shows normalised source 3-hase voltages which are the input voltages of the autotransformer. The normalised 3-phase supply voltages are plotted for comparison.

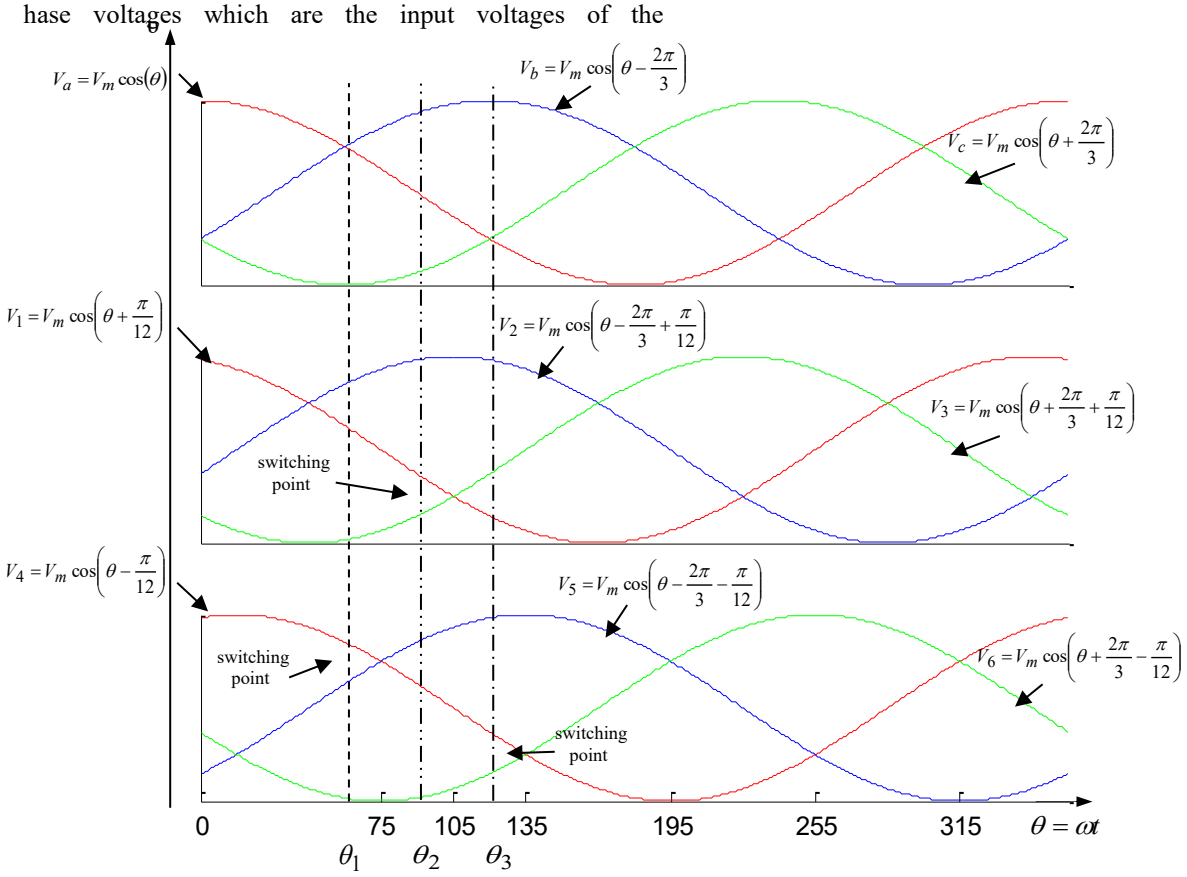

Figure 7. The cutting machine under study

Fig 7: Input and output 3-phase voltages of the autotransformer

Since the two rectifier outputs are not isolated, two IPRs must be used to prevent the flow of circulating currents. Assuming that the two rectifiers share the load current equally, the constant k_o in (10) and (11) is again 0.5, however, D will now have the value of 2 L_{ipr}. The expressions for the terms in equation (5) for this circuit are derived in Previous article and the results are:

	Autotransformer-based rectifier		
A	$+\frac{1}{2}(1+\frac{1}{\sqrt{3.27}})$	$-\frac{3}{4}(1+\frac{1}{.267})$	$-(1+\frac{1}{\sqrt{3.27}})$
B1	$+\frac{1}{2}(1+\frac{1}{\sqrt{3.27}})$	$-\frac{3}{4}(1+\frac{1}{.267})$	$-(1+\frac{1}{\sqrt{3.27}})$
B2	$-(1+\frac{1}{\sqrt{3.27}})$	$-(1+\frac{1}{\sqrt{3.27}})L_p+\frac{3L_s}{4}$	$((1+\frac{1}{.26})L_p+\frac{3L_s}{4})$
B3	$\frac{-4L_p}{\sqrt{3.27}}$	$+((1+\frac{1}{.26})L_p+\frac{L_s}{2})$	$-(1+\frac{1}{.26})L_p+\frac{3L_s}{4}$
B4	$[\ (1+\frac{4L_p}{\sqrt{3.27}})$	$(1+\frac{.26}{\sqrt{3}})L_p+3L_s$	$-((1+\frac{3.73}{\sqrt{3.27}})L_p+3L_s)\ ]$

B5	$+\frac{1}{2}(1+\frac{1}{\sqrt{3.27}})$	$-\frac{3}{4}(1+\frac{1}{.267})$	$-(1+\frac{1}{\sqrt{3.27}})$	
B6	$-(1+\frac{1}{\sqrt{3.27}})$	$-(1+\frac{1}{\sqrt{3.27}})L_p+\frac{3L_s}{4}$	$((1+\frac{1}{.26})L_p+\frac{3L_s}{4})$	
B7	$\frac{-4L_p}{\sqrt{3.27}}$	$+((1+\frac{1}{.26})L_p+\frac{L_s}{2})$	$-(1+\frac{1}{.26})L_p+\frac{3L_s}{4}$	
B8	$[\ (1+\frac{4L_p}{\sqrt{3.27}})$	$(1+\frac{.26}{\sqrt{3}})L_p+3L_s$	$-((1+\frac{3.73}{\sqrt{3.27}})L_p+3L_s)\ ]$	
B9	$+\frac{1}{2}(1+\frac{1}{\sqrt{3.27}})$	$-\frac{3}{4}(1+\frac{1}{.267})$	$-(1+\frac{1}{\sqrt{3.27}})$	
B10	$-(1+\frac{1}{\sqrt{3.27}})$	$-(1+\frac{1}{\sqrt{3.27}})L_p+\frac{3L_s}{4}$	$((1+\frac{1}{.26})L_p+\frac{3L_s}{4})$	
B11	$\frac{-4L_p}{\sqrt{3.27}}$	$+((1+\frac{1}{.26})L_p+\frac{L_s}{2})$	$-(1+\frac{1}{.26})L_p+\frac{3L_s}{4}$	
B12	$[\ (1+\frac{4L_p}{\sqrt{3.27}})$	$(1+\frac{.26}{\sqrt{3}})L_p+3L_s$	$-((1+\frac{3.73}{\sqrt{3.27}})L_p+3L_s)\ ]$	
B13	$+\frac{1}{2}(1+\frac{1}{\sqrt{3.27}})$	$-\frac{3}{4}(1+\frac{1}{.267})$	$-(1+\frac{1}{\sqrt{3.27}})$	
B14	$-(1+\frac{1}{\sqrt{3.27}})$	$-(1+\frac{1}{\sqrt{3.27}})L_p+\frac{3L_s}{4}$	$((1+\frac{1}{.26})L_p+\frac{3L_s}{4})$	
B15	$\frac{-4L_p}{\sqrt{3.27}}$	$+((1+\frac{1}{.26})L_p+\frac{L_s}{2})$	$-(1+\frac{1}{.26})L_p+\frac{3L_s}{4}$	
B16	$[\ (1+\frac{4L_p}{\sqrt{3.27}})$	$(1+\frac{.26}{\sqrt{3}})L_p+3L_s$	$-((1+\frac{3.73}{\sqrt{3.27}})L_p+3L_s)\ ]$	
C	$\frac{3L_p}{4\sqrt{3.27}}$	$-(1+\frac{1}{\sqrt{3.27}}\frac{L_p}{4}+\frac{3L_s}{4})$	$((1+\frac{1}{\sqrt{3.27}})\frac{L_p}{4})$	
θ_1,θ_2, IPR, i	$\frac{\pi}{3}-\frac{\pi}{36}$	$\frac{\pi}{2}-\frac{\pi}{36}$	$16L_{IPRr}$	$i_L/16$

Substituting the values into (13) and simplifying yields the final expression for the average output voltage of the rectifier.

$$\overline{V_r}=\frac{192\sqrt{3}}{\pi}\sin\left[\frac{\pi}{12}\right]V_m-\left[\frac{48\omega}{2\pi}\left(2\left(1-\frac{3}{k}\right)L_p+L_s\right)\right]\bar{i}_r$$
$$-\left[2L_p+L_s+2L_{ipr}\right]\frac{d\bar{i}_r}{dt}-\left[2r_p+r_s\right]\bar{i}_r \qquad (20)$$

The result in (20) again has the same form of the other results and Fig. 4 shows the equivalent circuit. The expressions for the component values in the equivalent circuit are given in Table 3.

Table 3. Terms of the averaged model of an autotransformer-based, 96-pulse rectifier

V_{eq}	R_{eq}	L_{eq}
$\frac{192\sqrt{3}}{\pi} sin\left(\frac{\pi}{12}\right) V_m$	$\frac{48\omega}{2\pi}\left(n^2 L_p + L_s\right) + \left[\left(1+\frac{\sqrt{3}}{2}\right) n^2 r_p + r_s\right]$	$\left[2L_p + L_s\right] + 2L_{ipr}$

7. Comparison of models

Comparing the averaged models for the two transformer coupled rectifiers, (20) and (19), and Tables 1 and 2, it is seen that the no load voltage is doubled in the series connected configuration and the effects of the primary and secondary inductances are four times larger. However, for the parallel-connected rectifier the leakage inductance of the IPR provides an additional series inductance in the equivalent circuit.

Comparing the averaged model of the two parallel connected rectifiers, equations (20) and (19), and Tables 2 and 3, if the voltage ratio of the doubly wound transformer *n* set to unity, the no-load output voltages are slightly different, the voltage is $1/cos\left(\pi/96\right)$ higher for the autotransformer based system, which is the output-to-input voltage ratio of the autotransformer. Also, in the autotransformer based circuit the values of the series inductance and overlap resistance terms are both $1/cos^2\left(\pi/96\right)$ bigger than in the doubly wound case. This suggests that the model for the autotransformer based rectifier is a special case of parallel connected rectifier model, with the turns ratio *n* set to $1/cos\left(\pi/96\right)$. However, in Chapter 4 it will be shown that there are important differences between the two rectifiers in terms of the way they interact in multi –rectifier systems. In addition the autotransformer-based system has increased output impedance due to the requirement for two inter-phase reactors.

Comparing the averaged models of 96-pulse rectifiers of this chapter with averaged model of a 48-pulse rectifier which is studied in paper 72, the 948 pulse rectifiers of this chapter are made by using two 48-pulse rectifier outputs in parallel or in series, therefore the no load output voltages of them are the same as a 48-pulse one or twice of it.

8. Results from prototype tests and Simulation works

To validate the averaged models of the rectifiers, the results from the equivalent circuits are compared with those from detailed circuit simulations undertaken in Micro-Cap SPICE. For the autotransformer configuration, experimental results are included. The circuits are discussed in turn in the following sections.

9. Series Y/ZYZΔ connection

Table 4 shows the component values of the test system for the series-connected Y/ZYZΔ rectifier circuit. To verify the model a transient response to a step increase in load power from 500 W to 1 kW at time 0.06 sec was performed.

Table 4. Component values of the test system

Parameter	V_m	f_s	L_p	r_p	L_s	r_s	L_{DC}	R_{DC}	C_{DC}
Unit	V	Hz	μH	mΩ	μH	mΩ	mH	mΩ	μF
Value	162	400	160	3.750	73	100	1.2	200	40

For these component values the overlap angle for 500W is 4.9°and for 1kW is 7°. This is based on the numerical solution described in Previous article. The analysis in paper72, shows that, these values of overlap cause 2% and 3% reduction in the values of the averaged model inductor and resistor, which are considered sufficiently small to be neglected, confirming the validity of the assumption in section 2.2.

The results from the detailed simulation and the averaged model are shown overlaid to facilitate close comparison. Fig. 8 a) shows the DC output voltage, V_{DC}, and Fig. 8 b) shows the DC link current i_r. The results show excellent prediction by the model of the DC-link transient. The natural frequency and the damping agree very closely. However, due to the averaging process, the model does not include any of the 96-pulse ripples seen in the detailed simulation.

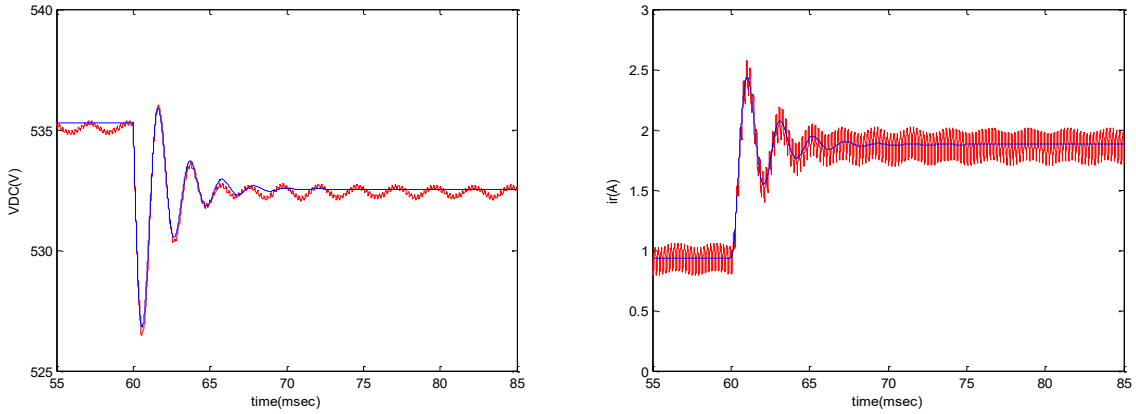

a) Capacitor voltage b) inductor current

Figure 8. Averaged value calculation and detailed simulation of DC-link capacitor voltage and inductor current of a 96-pulse Y/ZYZ□ series-connected rectifier

10. Parallel Y/ZYZΔ connection

Table 5 shows the component values of the test system for the parallel-connected Y/ZYZΔ rectifier circuit. In comparison with the series connection there is an extra parameter L_{ipr}, the leakage inductance of IPR, referred to the output side.

Table 5. Component values of the test system

Parameter	V_m	f_s	L_p	r_p	L_s	r_s	L_{ipr}	L_{DC}	R_{DC}	C_{DC}
Unit	V	Hz	μH	mΩ	μH	mΩ	μH	mH	mΩ	μF
Value	162	400	160	3.750	73	100	90	1.2	200	40

A transient response to a step increase in the load power from 500W to 1 kW at time 0.06 sec was performed. Similar to the series configuration in section Series Y/ZYZΔ connection, for these component values, the overlap angle for 500W is 4.9°and for 1kW is 7°. These values of overlap angle according to the analysis in section 2-2 of paper 48 are small enough to be neglected confirming the validity of the initial analysis assumptions.

Fig. 9 a) shows the DC output capacitor voltage, V_{DC}, and Fig. 9 b) shows the DC link inductor current i_r. The results show that there is a good match between the detailed simulation and the averaged model of the rectifier in terms of the response to a change at the load value. In comparison with the series connection, section 3.4.1 although the load value is the same, there is less damping in parallel configuration. One reason of that is the presence of less overlap damping resistor in parallel case since impedances are connected in parallel and another reason is because of presence of smaller small-signal resistance of the load for the parallel case.

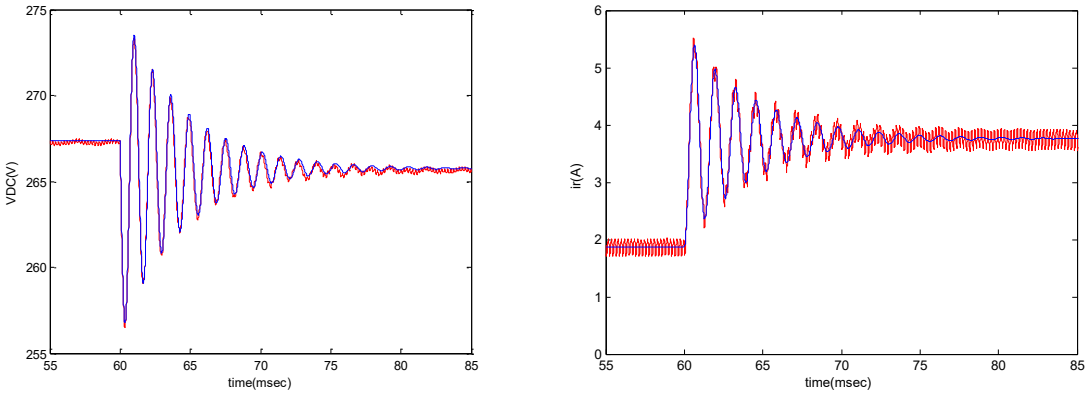

a) Capacitor voltage b) inductor current

Figure 9. Averaged value calculation and detailed simulation of DC-link capacitor voltage and inductor current of a 96-pulse Y/ZYZ□ parallel-connected rectifier

11. Autotransformer configuration

A prototype test system was used to verify the averaged model of the autotransformer based 96-pulse rectifier. The test system consisted of a variable voltage, variable frequency, 3-phase power supply, an autotransformer, a 3-phase full-bridge rectifier, 16 IPRs, and a DC-DC converter with resistive load. Full design details for the prototype test system are presented in paper 72. A detailed simulation of the circuit was run in micro-cap to compare with the averaged model. In the simulation the forward voltage drop of the diodes and also all the measured parameters of the autotransformer and IPRs, presented in Chapter 6, were included.

The system was tested under different circuit conditions such as different load values and different source voltage amplitudes and frequencies. Comparisons of the averaged model results with detailed simulation and experimental results are presented to show the model accuracy under different conditions.

Table 6 shows the parameter values of the system for the first test. The tested circuit was the circuit shown in Fig 6 including three extra inductors between power supply and rectifier to represent the transmission line. The parameters L_{p1} and r_{p1} show the value of the inductance and resistance of the added line inductors.

Table 6. Component values of the autotransformer-based, 96-pulse rectifier test system

Parameter	V_m	f_s	L_p	r_p	L_{p1}	r_{p1}	L_s	r_s	L_{DC}	R_{DC}	C_{DC}	V_O	R_L
Unit	V	Hz	μH	mΩ	μH	mΩ	μH	mΩ	μH	mΩ	μF	V	Ω
Value	270	800	160	3.750	60	98	21	310	600	13.75	52	90	22

Fig. 10 shows a comparison between the averaged model and a) detailed simulation and b) experimental results for the same circuit. The figure shows the DC link capacitor voltage and the filter inductor current.

A load resistor change was imposed on the output of the constant power regulated buck converter at t=0.06 s, a 14Ω load was added to the initial 22Ω resistor. Because the converter output voltage was regulated to a constant value of 90 V, a step change of 580 W was produced to the initial load value of 368 W.

The results show a good prediction by the model of the transient. Due to the averaging process, there is no ripple in the averaged model. As explained in paper 72, the steady-state voltage level difference between the experimental results and the model is attributed to the use of the high frequency value of the power supply output resistance in the model, giving accurate prediction of the damping of the transient.

The test was repeated for the same circuit for different source voltages and frequencies to verify the accuracy of the model for different operating points. Fig. 11 shows the results of the same test with different filter capacitor (72 μF) and the filter inductor (2.42 mH) and the filter resistor (400 mΩ) in comparison with the results of Fig. 10. The results

show that by increasing the value of the filter inductor the damping of the system transient decreased although the increment of the inductor resistance and the filter capacitor increases the damping of the system, but it seems in this case the increment of the filter inductor value had more effect in the system dynamic. In Fig. 12, the test condition was the same as Fig. 11; except that the source frequency was 400 Hz and filter capacitor was 52 µF. In this case the system damping decreased dramatically. This was because decrease of the source frequency and decrease of the filter capacitor value, both decrease the system damping.

In all above cases the results of the averaged model are follow the results of the detailed simulation and the experimental tests, accurately. This confirms the accuracy of the model for the prediction of dynamic interaction effects between the AC supply and the DC load.

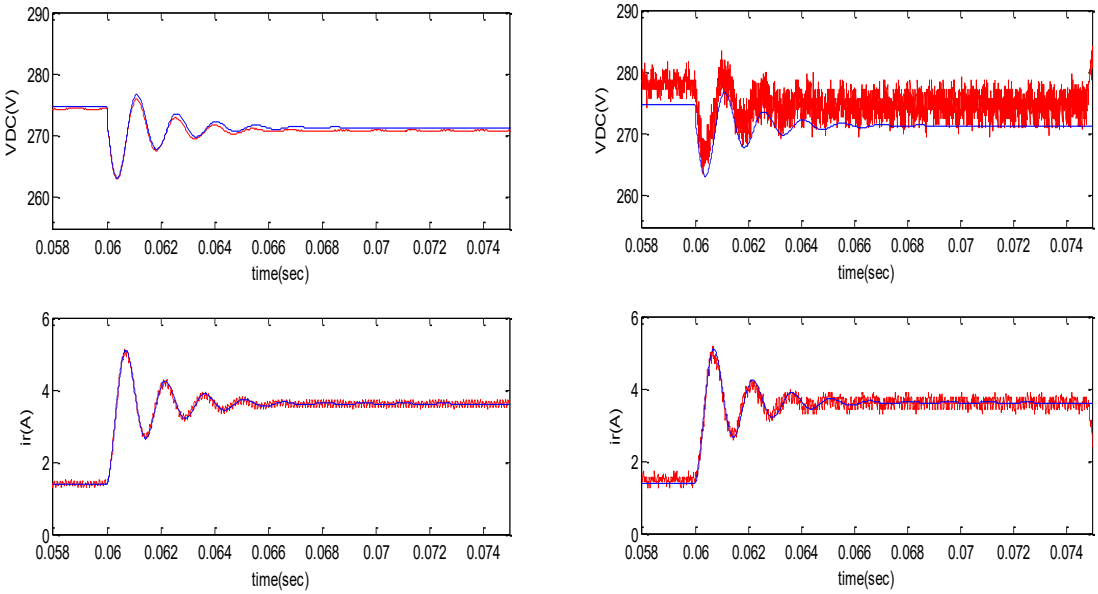

a) Detailed simulation b) Experimental results

Figure 10. A comparison between averaged model and detailed simulation, and between averaged model and experimental results for an autotransformer-based, 96-pulse rectifier

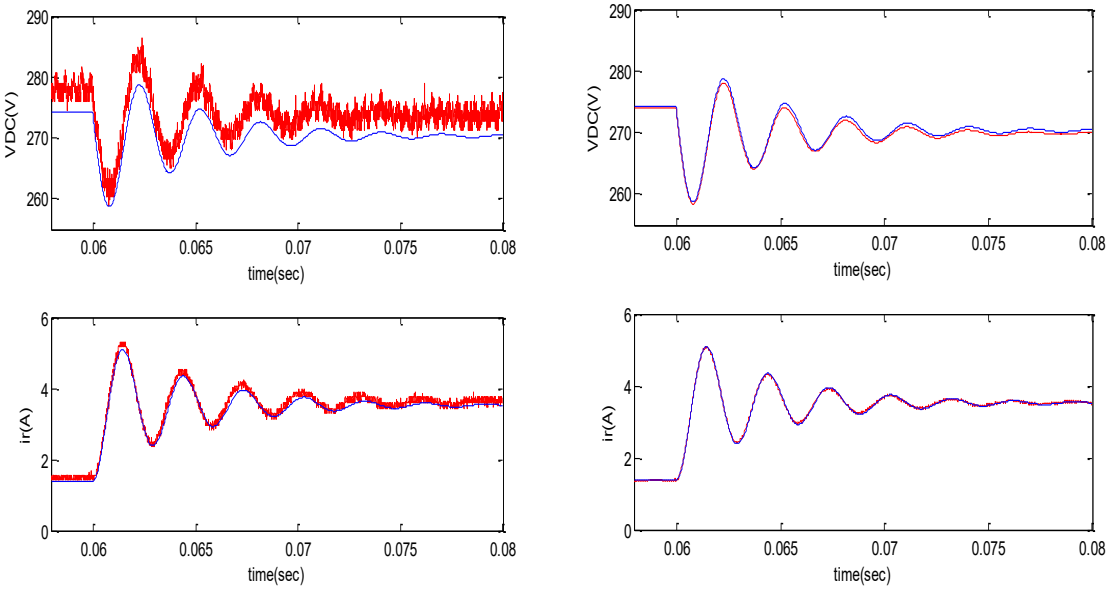

a) Detailed simulation b) Experimental results

Figure 11. A comparison between averaged model and detailed simulation, and between averaged model and experimental results for an autotransformer-based, 96-pulse rectifier (f=800 Hz, LDC =2.42 mH and RDC =400 mΩ and C=72 µF)

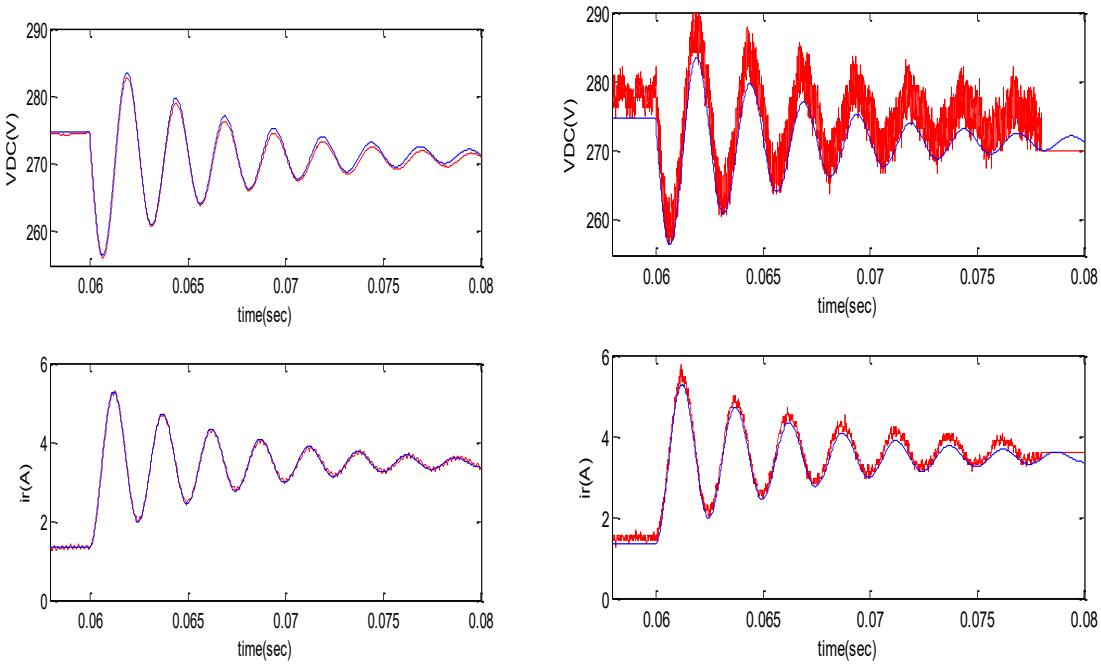

a) Detailed simulation b) Experimental results

Figure 12. A comparison between averaged model and detailed simulation, and between averaged model and experimental results for an autotransformer-based, 96-pulse rectifier (f=400 Hz, LDC =2.42 mH and RDC =400 mΩ and C=52 μF)

12. Summary

DC-side, averaged-value models have been derived for three common 96-pulse rectifiers, the autotransformer configuration being of particular interest for size/weight critical applications such as in the more-electric aircraft. In comparison, the model of the doubly-wound, transformer-based, 96-pulse rectifier with a ratio of $1/\cos(\pi/96)$ on the transformer output, is the same as the averaged model of an autotransformer based 96-pulse rectifier except that in the autotransformer based circuit there is an extra output inductance due to the requirement for two inter-phase transformers. Also, the equivalent circuit of a multi-rectifier system has been derived. The models have been validated by comparison with detailed circuit simulation; and for the autotransformer based rectifier the prototype test results confirmed the models.

13. Conclusion

This study presented the development and validation of nonlinear averaged-value models for three representative 96-pulse rectifier topologies—series-connected Y/ZYZ transformer-based, parallel-connected Y/ZYZ transformer-based, and autotransformer-based configurations—aimed at achieving accurate harmonic suppression and dynamic analysis in aerospace and HVDC applications. The proposed models were shown to effectively capture the essential DC-side dynamics by incorporating the influence of transformer leakage inductances, line resistances, and interphase reactor characteristics, while significantly reducing the computational complexity compared to detailed circuit simulations. Validation against Micro-Cap SPICE simulations and experimental prototype tests confirmed the models' capability to predict both steady-state operating conditions and transient responses with only minor deviations, mainly due to the exclusion of high-frequency ripple. The comparative analysis highlighted the trade-offs among the topologies, showing the autotransformer-based system offers weight and size advantages at the expense of galvanic isolation, while the series and parallel transformer-based systems provide design flexibility with different impedance characteristics. Overall, the results demonstrate that the proposed averaged-value models are reliable analytical tools for the design, optimization, and integration of high-pulse rectifiers in More Electric Aircraft power systems, uninterruptible power supplies (UPS), and HVDC networks. Future research may extend these models to

hybrid rectifier–converter systems, incorporate active interphase reactors, and explore advanced control strategies to further enhance power quality and system stability

Authors' Contributions

Authors equally contributed to this article.

Acknowledgments

Authors thank all participants who participate in this study.

Declaration of Interest

The authors report no conflict of interest.

Funding

According to the authors, this article has no financial support.

Ethical Considerations

All procedures performed in this study were under the ethical standards.

References

[1] A. Alahmad, F. Kacar, and C. P. Uzunogl, "Optimum design of an 18-pulse phase shifting autotransformer rectifier to improve the power quality of cascaded H-bridge motor driver," *Elektronika Ir Elektrotechnika,* vol. 29, no. 6, pp. 12-18, 2023.

[2] Y. Gao, X. Wang, and X. Meng, "Advanced Rectifier Technologies for Electrolysis-Based Hydrogen Production: A Comparative Study and Real-World Applications," *Energies,* vol. 18, no. 1, p. 48, 2024.

[3] S. Karmakar and B. Singh, "96-pulse VSC based large-scale grid interfaced solar PV plant with distributed MPPT and DC-coupled battery energy storage," in *2022 IEEE Global Conference on Computing, Power and Communication Technologies (GlobConPT)*, IEEE, 2022/09 2022, pp. 1-6.

[4] A. Alahmad, F. Kaçar, and C. P. Uzunoğlu, "Medium voltage drives (MVD)–design and configuration of eighteen-pulse phase shifting autotransformer rectifier for cascaded H-bridge motor driver application," *Electric Power Components and Systems,* pp. 1-8, 2024.

[5] S. Karmakar and B. Singh, "48-pulse voltage-source converter based on three-level neutral point clamp converters for solar photovoltaic plant," *IEEE Journal of Emerging and Selected Topics in Power Electronics,* vol. 10, no. 5, pp. 5894-5903, 2022.

[6] H. Wang, S. Tao, Y. Xu, Y. Long, and Z. Zhuang, "Load Regulation Margin Analysis for Aluminum Electrolysis Based on Operational State Identification," in *2023 2nd Asia Power and Electrical Technology Conference (APET)*, IEEE, 2023/12 2023, pp. 767-774.

[7] M. S. H. Lipu *et al.*, "Review of electric vehicle converter configurations, control schemes and optimizations: Challenges and suggestions," *Electronics,* vol. 10, no. 4, p. 477, 2021.

[8] K. A. Young, "Comparative analyses of multi-pulse phase controlled rectifiers in continuous conduction mode with a two-pole lc output filter for surface ship DC applications," Naval Postgraduate School, Monterey, CA, 2013.

[9] M. Mohan, B. Singh, and B. Ketan Panigrahi, "Design, control, and modeling of a new voltage source converter for HVDC system," *International Journal of Emerging Electric Power Systems,* vol. 14, no. 2, pp. 123-138, 2013.

[10] M. Brůha, *Moderní koncepce pohonů středních a velkých výkonů*. 2018.

[11] T. E. D. Meschede, *AOM (acousto-optical modulator) 114, 306 aperture aberration 173 argon laser 261 astigmatism 174*. 2017.

[12] L. Setlak, R. Kowalik, and T. Lusiak, "Practical use of composite materials used in military aircraft," *Materials,* vol. 14, no. 17, p. 4812, 2021.

[13] Z. Xu *et al.*, "Stability-oriented impedance modeling, analysis, and shaping for power supply system in more-electric aircraft: A review," *IEEE Transactions on Transportation Electrification,* vol. 10, no. 4, pp. 9351-9365, 2024.

[14] J. Overbeck, "Development and application of NMR methods to study biomolecular dynamics," 2023.

[15] J. Kaur and S. K. Bath, "Harmonic distortion in power systems due to electronic control and renewable energy integration: a comprehensive review," *Discover Electronics,* vol. 2, no. 1, p. 67, 2025.

[16] L. Lun, S. Chen, Y. Zhan, H. Yang, and J. Zhu, "A Harmonic Suppression Method for the Single Phase PWM Rectifier in the Hydrogen Production Power Supply," *Applied Sciences,* vol. 15, no. 7, p. 3978, 2025.